PHYSICAL REVIEW B **81**, 081401(R) (2010)

Oxygen vacancy induced structural variations of exfoliated monolayer MnO_2 sheets

Yong Wang,[1] Chenghua Sun,[2,3] Jin Zou,[1,4,*] Lianzhou Wang,[2,5] Sean Smith,[3] G. Q. Lu,[2,†] and David J. H. Cockayne[6]
[1]*Materials Engineering, The University of Queensland, St. Lucia, Queensland 4072, Australia*
[2]*ARC Centre of Excellence for Functional Nanomaterials, AIBN, The University of Queensland, St. Lucia, Queensland 4072, Australia*
[3]*Centre for Computational Molecular Science, The University of Queensland, St. Lucia, Queensland 4072, Australia*
[4]*Centre for Microscopy and Microanalysis, The University of Queensland, St. Lucia, Queensland 4072, Australia*
[5]*Chemical Engineering, The University of Queensland, St. Lucia, Queensland 4072, Australia*
[6]*Department of Materials, University of Oxford, Parks Road, Oxford OX1 3PH, United Kingdom*
(Received 8 January 2010; published 3 February 2010)

We report findings on the structural stability of exfoliated monolayer MnO_2 sheets. Our study reveals that monolayer MnO_2 sheets display two specific kinds of structural modification under electron irradiation. An atomic reconstruction (2×1) and a phase of MnO, induced by ordered oxygen vacancies, were identified by transmission electron microscopy techniques and further characterized by comparison with density-functional theory calculations. These findings are expected to significantly broaden current knowledge of the structural stability of ultrathin layered sheets.

DOI: 10.1103/PhysRevB.81.081401 PACS number(s): 64.70.Nd, 68.35.B−, 68.37.Lp, 31.15.E−

Single atomic-layered crystalline sheets, particularly graphene, have attracted significant attention recently due to their unique two-dimensional (2D) structures and new physicochemical properties.[1–6] Strictly speaking, no perfect 2D crystalline sheet structure would exist in free space unless it became an inherent part of a bulk crystal.[7–10] It has been demonstrated that suspended graphene sheets are not perfectly flat but exhibit intrinsic microscopic corrugations or ripples out of their 2D planes.[8,10] In addition to graphene, metal oxide monolayer sheets derived from delamination of layered transition metal oxide compounds represent a class of 2D nanostructures which are scientifically interesting as well as having potentially very important technological applications.[11,12] However, until now, little has been known about the degree of stability of these suspended monolayer (atomic or molecular) sheets possessing extremely large surface area and, if structural variations do occur, what types of structures could result. Undoubtedly, knowledge about the stability of these monolayer sheets will play a vital role in interpreting their properties[1–4] and in exploring their potential applications.[5,13]

Atomic structures and reconstructions on surfaces of single crystals have been studied for more than 20 years since the noted 7×7 Si (111) surfaces were discovered[14–16] and atomic structures of single-walled carbon nanotubes [one-dimensional (1D)] have also been investigated extensively.[17–19] More recently, Ishigami *et al.*[7] reported the atomic structure of graphene formed on a SiO_2 substrate. They observed both triangular and hexagonal lattices in the scanning tunneling microscopy images and suggested that the formation of these structures could be attributed to the film curvature and/or charge traps on the SiO_2 surface.

On the other hand, Meyer *et al.*[8] and Stankovich *et al.*[9] revealed significant local curvature within graphene and suggested that this curvature was caused by the lattice deformations. Nevertheless, no direct evidence of atomic reconstructions was provided with respect to these monolayer (molecular or atomic) sheets, limiting the pace of progress toward understanding their stability or the mechanism for their corrugations or curvatures. In fact, for 2D sheets with large numbers of surface atoms (i.e., on both faces) and likewise adatoms,[20] the atomic reconstructions or ordered rearrangements, if occurring, will not necessarily be similar to their three-dimensional (3D) crystalline counterparts. For the crystalline surface the layer underneath exerts a large influence on the surface reconstructions.

One powerful way to investigate the stability of these layered structures is to subject them to electron irradiation. This approach has led to the discovery of spherical carbon onions resulting from electron irradiation of graphitic soot,[21] the observation of the nucleation and growth of diamonds inside carbon onions under electron irradiation,[22] and more recently, the observation of reconstructions in (110) surfaces of an ultrathin TiO_2 films processed by ion beam thinning.[23] For this reason, we employed the controlled electron irradiation using transmission electron microscopy (TEM) to investigate the stability and structural changes of hexagonal MnO_2 monolayer sheets suspended on holey carbon films without any further substrate support. The study reveals atomic reconstructions under the electron-beam irradiation, resulting in new ordered domains within the MnO_2 sheets which are stable over 2 h of irradiation.

Exfoliated monolayer MnO_2 nanosheets have been synthesized following early publications of one of our authors[24,25] and confirmed to be monolayer MnO_2 nanosheets by the atomic force microscopy measurement.[25] TEM experiments were carried out on a FEI Tecnai 12 TEM operating at 100 kV with a beam dose around 4×10^5 $e/\mathrm{nm}^2\,\mathrm{s}$ for selected area electron diffraction (SAED) and a Tecnai F30 TEM working at 300 kV with a beam dose around 6×10^5 $e/\mathrm{nm}^2/\mathrm{s}$ for high-resolution TEM (HRTEM) and electron-energy-loss spectroscopy (EELS). The SAED and HRTEM simulations were conducted on a commercial code, JEMS (by Pierre Stadelmann, Switzerland).

A typical TEM image of the exfoliated MnO_2 nanosheets is shown in Fig. 1(a). As reported in Ref. 24, the MnO_2 sheet has a 2D hexagonal unit cell with nominal lattice parameter of $a=2.84$ Å. From the side view, the MnO_2 sheet has three atomic layers (one Mn layer sandwiched by two O layers).

 ©2010 The American Physical Society

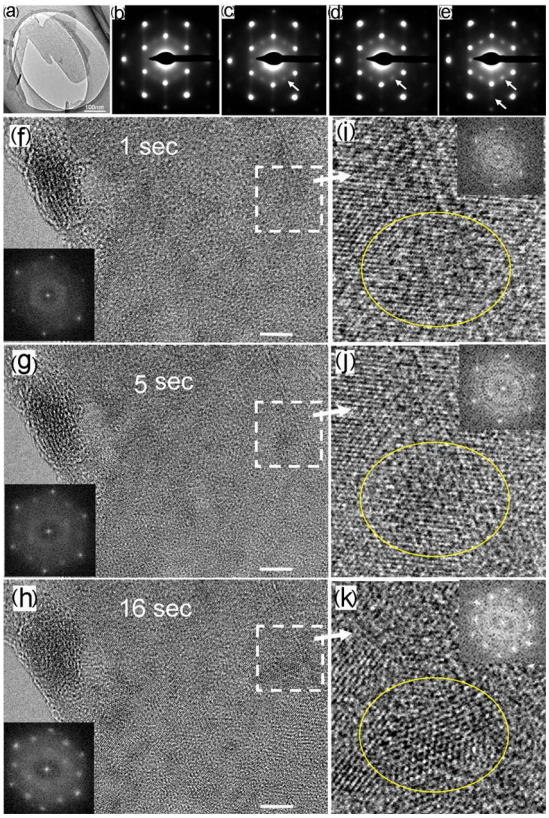

FIG. 1. (Color online) (a) A typical TEM image of a single MnO_2 sheet. Four SAED patterns acquired from this MnO_2 sheet with increasing electron-beam irradiation duration: (b) 1 s; (c) 2 min; (d) 10 min; and (e) 30 min. Three HRTEM images acquired from the same region with increasing electron-beam irradiation duration: (f) 1 s; (g) 5 s; and (h) 16 s. The insets are the corresponding FFT patterns. [(i)–(k)] are the magnified images of the areas marked (~10 nm in width) in (f)–(h), respectively. The scale bar is 5 nm.

However, since the distance between the Mn layer and O layers is only ~1.66 Å, we neglect the thickness of the entire sheet in further discussion but describe the monolayer MnO_2 sheet using the 2D coordinates, with the three atoms in a unit cell being located at Mn (0, 0); O_1 (1/3, 2/3); O_2 (2/3, 1/3) [refer to Fig. 4(a)].

Figures 1(b)–1(e) are the SAED patterns taken under different durations of electron irradiation (namely, 1 s, 2, 10, and 30 min, respectively), showing the effect of the electron-beam irradiation on the SAED patterns. As can be seen, extra diffraction spots appear after 2 min of irradiation and their intensities increase with increasing the irradiation duration (one such diffraction spot is marked by arrows in different SAED patterns). The appearance of these extra diffraction spots suggests that new structures (not just random crystal damage) have been formed during the electron-beam irradiation. To confirm this structural change, HRTEM investigations were carried out and the results are presented in Figs. 1(f)–1(k), in which HRTEM images from a local area of a 2D MnO_2 sheet were obtained at different durations of electron irradiation (namely, 1, 5, and 16 s, respectively). The insets are the corresponding fast Fourier transformation (FFT) patterns of the HRTEM images, which are similar to

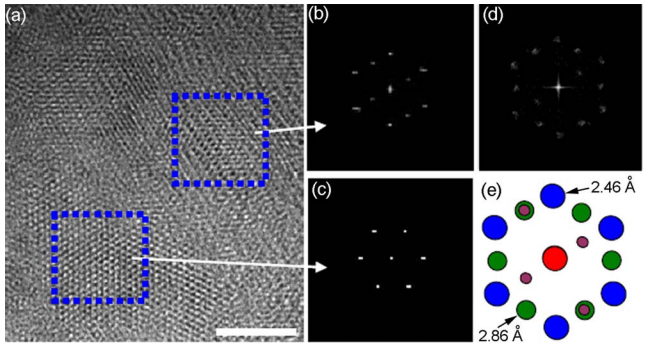

FIG. 2. (Color online) (a) HRTEM image of a typical MnO_2 sheets after irradiation showing two new structures (marked by squares). Scale bar=4 nm. (b) and (c) are their corresponding FFT patterns. (d) The FFT pattern of (a) showing superimposed different structures. (e) is a schematic drawing of (d).

the obtained SAED patterns [refer to Figs. 1(c)–1(e)]. As can be seen from the FFT patterns, extra diffraction spots were also observed for the 2D sheet which had experienced electron-beam irradiation. Furthermore, in Figs. 1(i)–1(k), one can clearly distinguish the structural changes in the marked regions at the atomic scale. To understand such structural variations in the monolayer MnO_2 sheets, we first concentrate on the SAED patterns. As shown in Fig. 1(e), the strong spots in this SAED pattern display a sixfold symmetry, which is expected to appear in the diffraction patterns taken along the normal (i.e., [001]) direction of hexagonal sheets (such as graphene sheets)[8,9] and the additional symmetrical weak spots induced by irradiation can also be clearly observed. It should be emphasized that this kind of SAED patterns is not unique to monolayer MnO_2 sheets. In fact, almost identical SAED patterns of graphene-based sheets have been reported recently.[9] In order to clarify the origin of the SAED patterns, extensive SAED and HRTEM investigations were carried out. A typical example is demonstrated in Fig. 2, in which two new structures (other than normal MnO_2) can be identified within one monolayer sheet, as marked by dashed squares in Fig. 2(a). Careful examination reveals that Fig. 2(b) shows a FFT pattern with a 2×1 reconstruction characteristic [also refer to Figs. 3(b) and 3(d)], however, Fig. 2(c) demonstrates a structure as it cannot be indexed by simple reconstruction [also refer to Figs. 4(h) and 4(j)]. Based on these results, we conclude that the SAED pattern arises from three types of 2D structures (or domains within the sheet): the normal hexagonal MnO_2 with a_0=2.84 Å [$d_{(10)}$=2.46 Å, blue spots in Fig. 2(e)]; its 2×1 reconstruction with a=5.68 Å and b=2.84 Å [Fig. 2(b)] [note that there are another 2 identical ones, which are rotated by 120° clockwise and anticlockwise with respect to Fig. 2(b), respectively] and finally a new hexagonal phase with a=5.72 Å [$d_{(10)}$=2.86 Å, Fig. 2(c) or green spots in Fig. 2(e), confirmed later].

To explain the diffraction pattern in Fig. 2(b), a 2×1 reconstruction model containing oxygen vacancies (OVs), as shown in Fig. 3(a), is proposed. The experimental FFT pattern is shown in Fig. 3(b). Diffraction patterns and HRTEM images simulated from this model are shown in Fig. 3(c) and the inset in Fig. 3(d), respectively. They are consistent with

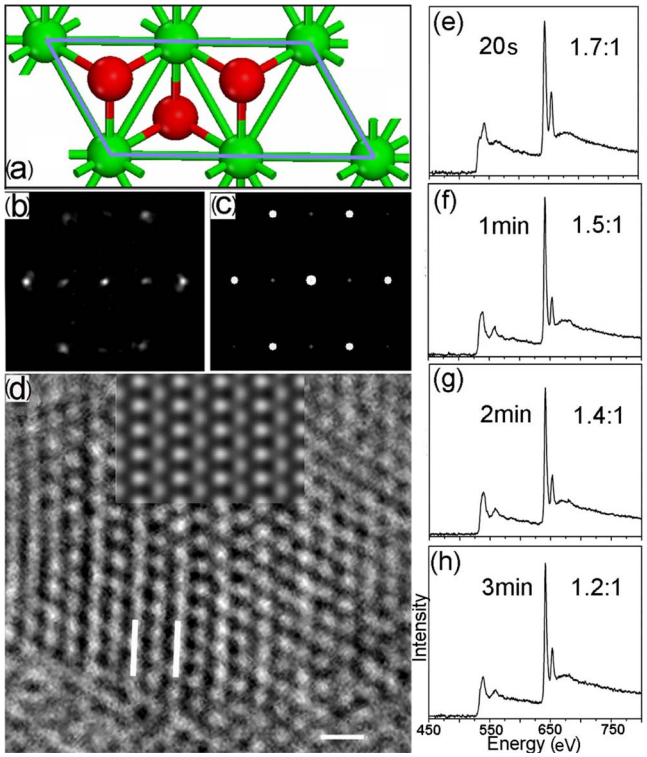

FIG. 3. (Color online) (a) the proposed model of the 2×1 reconstruction with $a=5.68$ Å, $b=2.84$ Å; (b) the experimental FFT pattern of (d); (c) the simulated diffraction pattern based on (a); (d) a typical HRTEM image of the 2×1 reconstruction—the inset shows the simulated HRTEM image, which agree with the experimental result with high fidelity. The distance between the two lines in (d) is 4.9 Å and the scale bar is 5 Å. [(e)–(h)] EELS results show O:Mn ratio changed from 1.7:1 to 1.2:1 after 3 min irradiation.

the experimental results, verifying that Fig. 3(b) can be reproduced based on a model incorporating OVs, as shown in Fig. 3(a). Indeed, EELS experiment confirms the loss of oxygen [Figs. 3(e)–3(h)]. To further investigate the stability of such OV-induced structures, spin-polarized density-functional theory (DFT) calculations were performed within the generalized-gradient approximation (GGA),[26] with the exchange-correlation functional of Perdew-Burke-Ernzerhof (PBE),[27] which has been implemented in the Vienna *ab initio* simulation package (VASP).[28] It was found that the framework of the model proposed in Fig. 3(a) retains its structural integrity very well during the optimization,[29] indicating the excellent stability of the proposed model. Collectively, the combination of experimental evidence from complementary techniques and theoretical results suggests strongly that the 2×1 reconstruction is caused by OVs, as shown in Fig. 3(a).

In contrast with the 2×1 reconstruction, the diffraction pattern shown in Fig. 2(c) cannot be explained simply as a reconstruction due to the missing of primary diffraction spots. The fact that this pattern is rotated 30° with respect to the normal hexagonal diffraction pattern [Fig. 2(e)] indicates that the translation vectors of the corresponding structure must have a 30° rotation when compared with the normal one. To satisfy this requirement, a smaller supercell, reproduced from a perfect MnO_2 nanosheet, can be drawn as the $(\sqrt{3}\times\sqrt{3})R30°$ supercell (indicated as Mn_3O_6), as shown in Fig. 4(a), with $a=\sqrt{3}a_0=4.92$ Å. On the other hand, the atomic spacings corresponding to these diffraction spots in Fig. 2(c) are $d=2.86$ Å [corresponding to $a=5.72$ Å based on the $(\sqrt{3}\times\sqrt{3})R30°$ supercell], rather than $d=2.46$ Å (corresponding $a=4.92$ Å) measured from Fig. 2(b).[30] This result suggests that the supercell could be expanded from $a=4.92$ Å to $a=5.72$ Å. To understand this and to understand the driving force for the lattice expansion, extensive EELS was carried out, from which it was found that there was considerable oxygen loss during electron-beam irradiation [Figs. 3(e)–3(h)], suggesting that such structural expansion could be induced by missing oxygen. To verify this hypothesis, DFT was employed to calculate the lattice constants for different oxygen concentrations. Practically, Fig. 4(a) was modified by introducing OVs with different concentrations, indicated as Mn_3O_x ($x=6, 5, 4, 3, 2, 1$), as shown in Figs. 4(a)–4(f). The lattice constants of Mn_3O_x were obtained by DFT optimization and the results are shown in Fig. 4(g). For Mn_3O_6 [Fig. 4(a)], the optimized value of $a=4.99$ Å is in agreement with the experimental value of 4.92 Å for the normal structure [indicated by the red circle in Fig. 4(g)], suggesting that accurate lattice constants can be determined from the computational method employed. As indicated in Fig. 4(g), both Mn_3O_3 and Mn_3O_4 give a lattice constant of 5.80 Å, which is in agreement with the experimental value of 5.72 Å for the new phase [indicated by the red dashed line in Fig. 4(g)]. From the optimized geometries of Mn_3O_4, it is further found that three of the four oxygen atoms move almost onto to the manganese plane, with the fourth oxygen adsorbed at the center of three manganese atoms, as shown in Fig. 4(c). In fact, Mn_3O_4 is essentially a hexagonal MnO monolayer with an oxygen adsorbed. In other words, the only difference between Figs. 4(c) and 4(d)

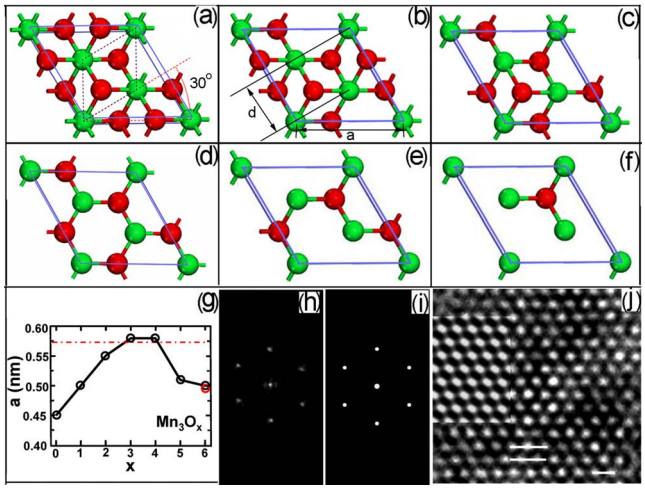

FIG. 4. (Color online) (a) Mn_3O_6 (O: red/gray, Mn: green/light gray); (b) Mn_3O_5; (c) Mn_3O_4; (d) Mn_3O_3; (e) Mn_3O_2; (f) Mn_3O_1; (g) DFT optimized lattice constants for Mn_3O_x ($x=6, 5, 4, 3, 2, 1, 0$); (h) experimental SAED; (i) simulated SAED based on Mn_3O_3 shown in (d); (j) experimental and simulated (inset) HRTEM images. The distance between the two lines in (j) is 2.86 Å and the scale bar is 5 Å.

is the additional adsorbed O atom above the Mn triad in Fig. 4(c). We then simulated the diffraction patterns and HRTEM images based on both Fig. 4(c) (Mn_3O_4) and Fig. 4(d) (Mn_3O_3) and found the same results, except for some very weak additional diffraction spots induced by the extra O in Fig. 4(c). This result suggests that the model of Fig. 4(d) is the likely case as we did not observe these weak diffraction spots in our experiments. Indeed, the simulated results from the model of Fig. 4(d) are consistent with the experimental results as shown in the comparison of Figs. 4(h) and 4(i). Experimentally, we find that the ratio of O/Mn (2:1 for perfect MnO_2) can be reduced to 1.2:1 after an electron irradiation of 3 min [Fig. 3(h)], indicating that oxygen atoms tend to leave the nanosheet surface under energetic perturbations of such an electron irradiation. Taking these results into account collectively, we suggest that the diffraction pattern in Fig. 2(c) is caused by the OV-induced MnO monolayer shown in Fig. 4(d).

In conclusion, through detailed combination of systematic TEM investigation and DFT calculations, we provide the demonstration of oxygen vacancy induced reconstruction and phase transformation of monolayer MnO_2 sheets under electron-beam irradiation. Future generations of electronic devices will increasingly exploit the unique physical, chemical, electronic, optical, and mechanical properties of nanostructures. Such properties are determined by the detailed atomic structures of these molecular architectures and the nuances of their electronic interactions. Both from the standpoint of fundamental scientific enquiry and technological imperatives, it is crucial in the case of monolayer sheets to extend knowledge of their dimensional stability as well as the propensity for structural rearrangements. The present Rapid Communication significantly advances insights into the structural stability of MnO_2 monolayer sheets and the principles elaborated herein may potentially be extended to other ultrathin functional nanosheets.

The Australian Research Council is acknowledged for its support to this Rapid Communication.

*j.zou@uq.edu.au

†maxlu@uq.edu.au

[1] Ç. Ö. Girit, J. C. Meyer, R. Erni, M. D. Rossell, C. Kisielowski, L. Yang, C. Park, M. F. Crommie, M. L. Cohen, S. G. Louie, and A. Zettl, Science **323**, 1705 (2009).

[2] K. S. Novoselov, A. K. Geim, S. V. Morozov, D. Jiang, M. I. Katsnelson, I. V. Grigorieva, S. V. Dubonos, and A. A. Firsov, Nature (London) **438**, 197 (2005).

[3] A. K. Geim and K. S. Novoselov, Nature Mater. **6**, 183 (2007).

[4] C. Berger, Z. M. Song, X. B. Li, X. S. Wu, N. Brown, C. Naud, D. Mayou, T. B. Li, J. Hass, A. N. Marchenkov, E. H. Conrad, P. N. First, and W. A. de Heer, Science **312**, 1191 (2006).

[5] E. Yoo, J. Kim, E. Hosono, H. Zhou, T. Kudo, and I. Honma, Nano Lett. **8**, 2277 (2008).

[6] Y. Zhang, Y. W. Tan, H. L. Stormer, and P. Kim, Nature (London) **438**, 201 (2005).

[7] M. Ishigami, J. H. Chen, W. G. Cullen, M. S. Fuhrer, and E. D. Williams, Nano Lett. **7**, 1643 (2007).

[8] J. C. Meyer, A. K. Geim, M. I. Katsnelson, K. S. Novoselov, T. J. Booth, and S. Roth, Nature (London) **446**, 60 (2007).

[9] S. Stankovich, D. A. Dikin, G. H. B. Dommett, K. M. Kohlhaas, E. J. Zimney, E. A. Stach, R. D. Piner, S. T. Nguyen, and R. S. Ruoff, Nature (London) **442**, 282 (2006).

[10] A. Fasolino, J. H. Los, and M. I. Katsnelson, Nature Mater. **6**, 858 (2007).

[11] T. Sasaki, Y. Ebina, Y. Kitami, M. Watanabe, and T. Oikawa, J. Phys. Chem. B **105**, 6116 (2001).

[12] Y. Oaki and H. Imai, Angew. Chem., Int. Ed. **46**, 4951 (2007).

[13] F. Banhart, Rep. Prog. Phys. **62**, 1181 (1999).

[14] G. Binnig, H. Rohrer, Ch. Gerber, and E. Weibel, Phys. Rev. Lett. **50**, 120 (1983).

[15] Q. K. Xue, T. Hashizume, J. M. Zhou, T. Sakata, T. Ohno, and T. Sakurai, Phys. Rev. Lett. **74**, 3177 (1995).

[16] C. H. Lanier, J. M. Rondinelli, B. Deng, R. Kilaas, K. R. Poeppelmeier, and L. D. Marks, Phys. Rev. Lett. **98**, 086102 (2007).

[17] T. W. Odom, J. L. Huang, P. Kim, and C. M. Lieber, Nature (London) **391**, 62 (1998).

[18] P. M. Ajayan, V. Ravikumar, and J. C. Charlier, Phys. Rev. Lett. **81**, 1437 (1998).

[19] A. Hashimoto, K. Suenaga, A. Gloter, K. Urita, and S. Iijima, Nature (London) **430**, 870 (2004).

[20] J. C. Meyer, C. O. Girit, M. F. Crommie, and A. Zettl, Nature (London) **454**, 319 (2008).

[21] D. Ugarte, Nature (London) **359**, 707 (1992).

[22] F. Banhart and P. M. Ajayan, Nature (London) **382**, 433 (1996).

[23] N. Shibata, A. Goto, S. Y. Choi, T. Mizoguchi, S. D. Findlay, T. Yamamoto, and Y. Ikuhara, Science **322**, 570 (2008).

[24] L. Z. Wang, K. Takada, A. Kajiyama, M. Onoda, Y. Michiue, L. Zhang, M. Watanabe, and T. Sasaki, Chem. Mater. **15**, 4508 (2003).

[25] Y. Omomo, T. Sasaki, L. Z. Wang, and M. Watanabe, J. Am. Chem. Soc. **125**, 3568 (2003).

[26] W. Kohn and L. J. Sham, Phys. Rev. **140**, A1133 (1965).

[27] J. P. Perdew, K. Burke, and M. Ernzerhof, Phys. Rev. Lett. **77**, 3865 (1996).

[28] G. Kresse and J. Furthmüller, Phys. Rev. B **54**, 11169 (1996).

[29] Geometry optimization was performed without any symmetry constraints for the 2×1 reconstruction. (a) Crystal constants were fixed to experimental data: $a=5.68$ Å, $b=2.84$ Å, $c=22.00$ Å, $\alpha=90°$, $\beta=90°$, $\gamma=120°$, and the binding energies is −39.33 eV; (b) crystal constants were fully optimized, the final results of the 2×1 reconstruction is $a=5.92$ Å, $b=3.02$ Å, $c=20.20$ Å, $\alpha=90°$, $\beta=90°$, $\gamma=120.6°$, and the binding energy is −39.41 eV.

[30] Relationship between plane spacing (d) and crystal constant (a) [refer to Fig. 4(b)]: since $d=d_{\text{Mn-Mn}}\times\frac{\sqrt{3}}{2}$ and $\frac{a/2}{d_{\text{Mn-Mn}}}=\frac{\sqrt{3}}{2}$, then $d=a/2$. When $d=2.46$ Å, $a=4.92$ Å; when $d=2.86$ Å, $a=5.72$ Å.